EDGE ARTICLE

Flat-on ambipolar triphenylamine/C_{60} nano-stacks formed from the self-organization of a pyramid-sphere-shaped amphiphile†

Wei-Wei Liang,‡ Chi-Feng Huang,‡ Kuan-Yi Wu, San-Lien Wu, Shu-Ting Chang, Yen-Ju Cheng and Chien-Lung Wang*

A giant amphiphile, which is constructed with an amorphous nano-pyramid (triphenylamine, TPA) and a crystalline nano-sphere (C_{60}), was synthesized. Structural characterization indicates that this pyramid-sphere-shaped amphiphile (**TPA–C_{60}**) forms a solvent-induced ordered phase, in which the two constituent units self-assemble into alternating stacks of two-dimensional (2D) TPA and C_{60} nano-sheets. Due to the complexity of the molecular structure and the amorphous nature of the nano-pyramid, phase formation was driven by intermolecular C_{60}–C_{60} interactions and the ordered phase could not be reformed from the **TPA–C_{60}** melt. Oriented crystal arrays of **TPA–C_{60}**, which contain flat-on TPA/C_{60} nano-stacks, can be obtained via a PDMS-assisted crystallization (PAC) technique. The flat-on dual-channel supramolecular structure of **TPA–C_{60}** delivered ambipolar and balanced charge-transport characteristics with an average μ_e of 2.11×10^{-4} cm^2 V^{-1} s^{-1} and μ_h of 3.37×10^{-4} cm^2 V^{-1} s^{-1}. The anisotropic charge-transport ability of the pyramid-sphere-shaped amphiphile was further understood based on the lattice structure and the lattice orientation of **TPA–C_{60}** revealed from electron diffraction analyses.

1. Introduction

Giant amphiphiles are synthesized by covalently binding various nm-sized molecular building blocks (or so-called molecular nanoparticles (MNPs)).[1] Their self-assembly processes are driven by competitive or cooperative physical interactions among the MNPs and are largely influenced by the preferred packing scheme of the constituent MNPs. The giant amphiphiles contain a wide range of emerging materials[1,2] such as sphere-cube,[1] sphere-board,[3–5] sphere-disc,[6–19] discotic-rod,[20,21] cube-disk,[22] and cube-board[23]-shaped amphiphiles. Among these giant molecules, those built with p-type and n-type conjugated moieties have attracted much attention, because of their potential applications as active units in supramolecular optoelectronics.[5,24,25]
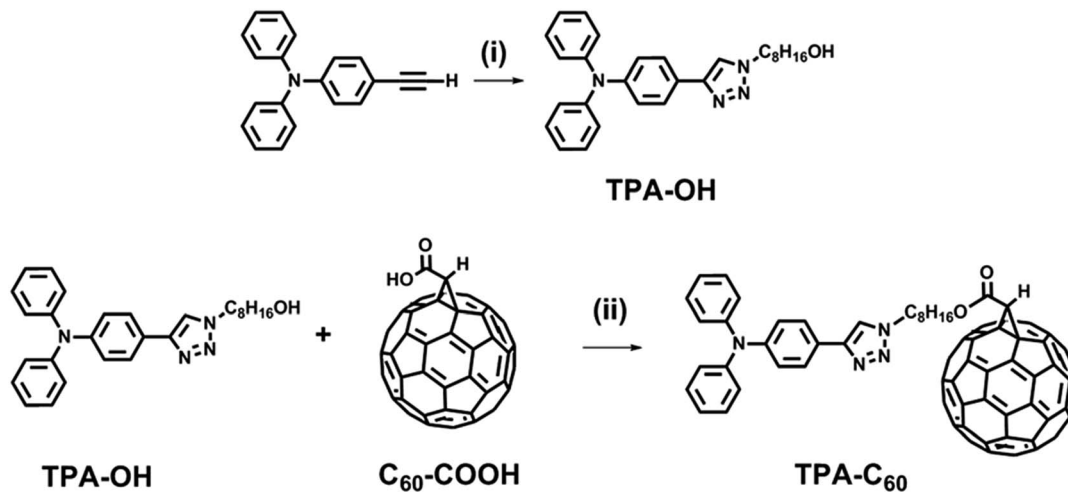
Giant molecules can be constructed from crystalline mesogenic, quasicrystalline and amorphous MNPs,[26] but so far, most giant amphiphiles are made with MNPs that are intrinsically crystalline. Triphenylamine (TPA)-based conjugated molecules are widely used in organic light emitting diodes (OLEDs),[27,28]

polymer solar cells (PSCs),[29] and perovskite solar cells,[30] because of their good morphological stability and p-type semi-conducting characteristics. However, they are rarely reported as MNPs of giant amphiphiles, probably due to their nonplanar structure and amorphous nature.[27,28] The incorporation of this pyramidal nano-building block raises interesting questions, such as whether the self-organization of a giant amphiphile will be compromised due to the presence of an amorphous nano-pyramid, or on the other hand, whether the amorphous nano-pyramid will self-organize because the other MNP of the giant amphiphile tends to crystallize. To explore these questions, a giant pyramid-sphere-shaped amphiphile, **TPA–C_{60}**, which is constructed with the amorphous nano-pyramid (TPA) and the crystalline nano-sphere (C_{60}), was designed and synthesized based on Steglich esterification and copper-catalyzed azide–alkyne cycloaddition (CuAAC), as shown in Scheme 1. The phase behavior and phase structure of **TPA–C_{60}** were investigated via differential scanning calorimetry (DSC) and electron diffraction (ED). The field effect transistor (FET) characteristics of **TPA–C_{60}** were evaluated with oriented **TPA–C_{60}** crystal arrays prepared via the PDMS-assisted crystallization (PAC) method.[31] The results show that the pyramid-sphere-shaped amphiphile self-organized into an ordered phase containing stacks of alternating two-dimensional (2D) C_{60} and TPA nanosheets. Moreover, this dual-channel supramolecular structure of **TPA–C_{60}** delivered ambipolar and balanced charge-transport characteristics in organic field-effect transistors (OFETs). Previous

Department of Applied Chemistry, National Chiao Tung University, 1001 Ta Hsueh Road, Hsin-Chu, 30010, Taiwan. E-mail: kclwang@nctu.edu.tw

Scheme 1 Synthetic route of **TPA–C$_{60}$**. Reagents and conditions: (i) 8-azidooctan-1-ol, copper(II) sulfate pentahydrate, sodium ascorbate, THF/H$_2$O (1/1, v/v); (ii) p-toluenesulfonic acid, 4-dimethylaminopyridine, 1-(3-dimethylaminopropyl)-2-ethylcarbodiimide hydrochloride, CS$_2$.

studies showed that TPA and C$_{60}$ have preferable physical interactions and tend to form a mixed TPA/C$_{60}$ domain in the solid-state.[32–34] However, with respect to functions, the mixed TPA/C$_{60}$ domain is not conducive to ambipolar charge transport. Our study thus gives the first example of flat-on ambipolar TPA/C$_{60}$ nano-stacks obtained *via* the self-organization of a pyramid-sphere-shaped amphiphile.

2. Results and discussion

2.1. Synthesis of TPA–C$_{60}$

Scheme 1 shows the synthetic route of **TPA–C$_{60}$**. 4-Ethynyl-*N,N*-diphenylaniline, 8-azidooctan-1-ol, and fullerenoacetic acid (**C$_{60}$-COOH**) were synthesized according to the literature.[35] Reacting 4-ethynyl-*N,N*-diphenylaniline with 8-azidooctan-1-ol *via* the CuAAC reaction allowed the formation of a p-type pyramid unit, 8-(4-(triphenylamino)-1*H*-1,2,3-triazol-1-yl)octan-1-ol (**TPA-OH**) in 67% yield. The final product, **TPA–C$_{60}$**, was then synthesized in 74% yield by reacting **TPA-OH** and **C$_{60}$-COOH** *via* Steglich esterification. **TPA–C$_{60}$** was characterized by ^{1}H NMR, ^{13}C NMR, and mass spectrometry. As shown in Fig. S1,† the formation of **TPA–C$_{60}$** was identified by the downfield shift of the methylene protons of **TPA-OH** (denoted as H$_a$ in Fig. S1†) and the appearance of a methine proton (H$_b$ in Fig. S1b†) at $\delta = 4.88$ ppm, which belongs to the C$_{60}$ moiety. The multiple peaks between $\delta = 135$ and 145 ppm in the ^{13}C-NMR spectrum of **TPA–C$_{60}$** (Fig. S2b†), are also characteristic of the sp^2 carbons on the mono-adduct C$_{60}$ moiety. Furthermore, as shown in Fig. S3,† the [M + H]$^+$ peak of the final product has an *m/z* value of 1201.267, which matches well with the calculated monoisotopic mass (1201.24 Da). All the results clearly indicate the success of the reaction and confirm the chemical identity and purity of **TPA–C$_{60}$**.

2.2. Thermal stability and phase transition

After vacuum drying using a cryo pump, thermogravimetric analysis (Fig. S4a†) showed a 5% weight loss temperature of

TPA–C$_{60}$ at 388 °C. As shown in Fig. S4b,† an additional weight loss peak at 131 °C was observed for a **TPA–C$_{60}$** sample that was only vacuum dried under a mechanical pump. The results indicate that the as-precipitated **TPA–C$_{60}$** contains residual solvent molecules that can be removed under high vacuum. DSC was then applied to identify the phase behaviour of the two MNPs and the pyramid-sphere-shaped amphiphile. As shown in Fig. S5a,† 4-ethynyl-*N,N*-diphenylaniline shows an endothermic first-order transition at 108 °C during the 1st heating, suggesting that the as-precipitated sample self-organized into an ordered phase. However, a corresponding exothermic transition in the subsequent cooling was not observed, indicating that 4-ethynyl-*N,N*-diphenylaniline was vitrified rather than crystallized during the cooling process. Consequently, in the 2nd heating (Fig. S5b†), the endothermic transition at 108 °C disappeared. As shown in Fig. S5c,† **TPA-OH** exhibits only a glass transition temperature at 10 °C. Thus, the results show the easily disturbed self-organization behaviour of the TPA unit, *i.e.* although 4-ethynyl-*N,N*-diphenylaniline self-organizes from the solution, this behaviour is lost in the melt and when a flexible alkyl group is attached. For **TPA–C$_{60}$**, three first-order transitions at 190, 226 and 239 °C were found in the 1st heating curve of **TPA–C$_{60}$** (Fig. S5d†), indicating that **TPA–C$_{60}$** packs into an ordered solid-state structure. The multiple transitions suggest that instead of directly transforming into the isotropic melt, the ordered phase of **TPA–C$_{60}$** may lose its structural order (conformational, orientational, and positional orders) in a stepwise way. In the cooling curve, no exothermic peak was observed, indicating that although self-organization of **TPA–C$_{60}$** from solution is possible, reforming the ordered packing from the melt is difficult, probably due to the structural complexity of **TPA–C$_{60}$**. In short, the DSC results revealed the amorphous nature of the alkylated TPA nano-pyramid and the crystalline characteristics of the **TPA–C$_{60}$** amphiphile. More importantly, it was found that the amorphous alkylated nano-pyramid (TPA) can self-assemble under the assistance of favourable intermolecular interactions among the crystalline nano-spheres (C$_{60}$).

2.3. Phase morphology of TPA–C$_{60}$

TPA–C$_{60}$ tends to form tiny crystals in drop-cast thin films. To obtain crystals large enough for device fabrication and to introduce better crystal orientation, the PAC method[31] was applied to produce a crystal array of TPA–C$_{60}$. Fig. 1 shows TPA–C$_{60}$ films obtained from different solvents. As shown in Fig. 1a and b, the crystal sizes were small when TPA–C$_{60}$ was processed from *m*-xylene and CS$_2$ solutions. However, the bright blue or yellow POM images suggested that TPA–C$_{60}$ has birefringence and structural order in the cast films. Large crystalline TPA–C$_{60}$ sheets were obtained from *o*-dichlorobenzene (ODCB) and 1,2,4-trichlorobenzene (TCB) solutions (Fig. 1c and d). Intriguingly, as shown in Fig. S6,† the color of the crystalline sheet was only observed when the incident light was polarized (Fig. S6c and d†) and the crystal does not turn dark even when its growth direction is along the polarization direction of the polarizer or the analyzer. A similar phenomenon was observed in the blue phases of highly chiral liquid crystals.[36] The origin of the blue or yellow POM images of TPA–C$_{60}$ falls outside the scope of the current study and will be investigated separately.

The AFM topography and cross-section profiles in Fig. 2 show that the TPA–C$_{60}$ film prepared from ODCB solution is a polycrystalline thin film with a very rough surface (max. thickness ∼ 80 nm), but the one prepared from TCB solution has an insignificant crystalline boundary and a uniform surface (thickness ∼ 150 nm). The crystal array prepared from TCB was further examined with transmission electron microscopy (TEM) and electron diffraction (ED). Similar to the AFM result, the TPA–C$_{60}$ crystal has a uniform appearance in the TEM image (Fig. 3a). The clear diffraction spots in the ED pattern (Fig. 3b) are evidence of the formation of an ordered solid-state structure, and more importantly, the well-oriented crystal lattices in the TPA–C$_{60}$ crystal array formed by the PAC method. These morphological characterization methods thus confirmed that the pyramid-sphere-shaped amphiphile, TPA–C$_{60}$, can assemble into an ordered phase, and a good lattice orientation can be induced *via* the PAC method.
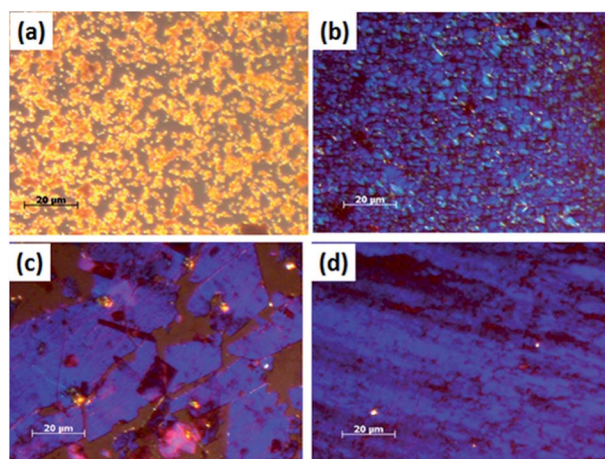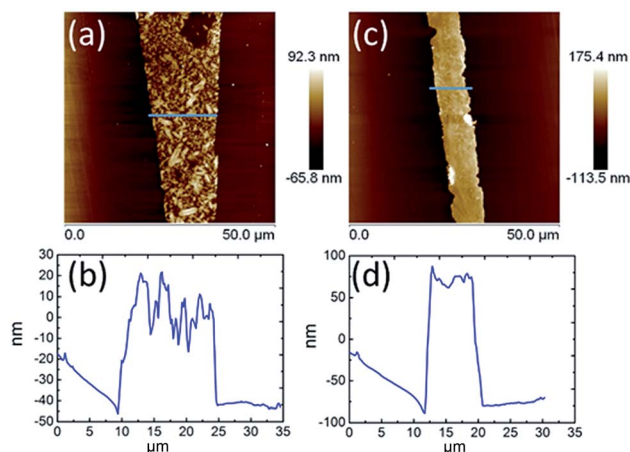

Fig. 2 AFM topography and cross-section profiles of TPA–C$_{60}$ processed *via* the PAC method with ODCB (a) and (b) and TCB (c) and (d).

2.4. Phase structure of TPA–C$_{60}$

Due to the structural complexity, preparation of a large single crystal of TPA–C$_{60}$ for single-crystal structural characterization was difficult. In addition, the ED patterns along different zone axes are still useful for revealing the 2D lattice projections of the TPA–C$_{60}$ crystal. Using the drop-cast sample, $a*b*$ and the $b*c*$ reciprocal lattices (Fig. 4b and c) were observed. The lattice parameters deduced from Fig. 4b are $a = 22.8$ Å, $b = 10.7$ Å, $\gamma = 90°$; and from Fig. 4c are $b = 10.7$ Å, $c = 51.0$ Å, and $\alpha = 90°$. The measured density of the TPA–C$_{60}$ crystal is 1.28 g cm^{-3}. Assuming that $\beta = 90°$, the density provides the information that the orthorhombic lattice ($a = 22.8$ Å, $b = 10.7$ Å, $c = 51.0$ Å, $\alpha = \beta = \gamma = 90°$) contains 8 TPA–C$_{60}$ molecules per unit cell. The powder X-ray diffraction (XRD) pattern of TPA–C$_{60}$ is shown in Fig. S7.† The theoretical *d*-spacings of various lattice planes calculated from the abovementioned lattice parameters also match the measured ones (Table S1†). Furthermore, the (100) and (010) diffractions in Fig. 4b are significantly weaker than the (200) and (020) diffractions, suggesting that in the lattice, the electron density on the (100) planes is close to that on the (200) planes and that on the (010) planes is similar to that on the (020) planes. A lattice model was then built using the Cerius^2 software package, based on the abovementioned information,

Fig. 1 POM images of TPA–C$_{60}$ processed *via* the PAC method with different solvents. (a) *m*-Xylene, (b) CS$_2$, (c) ODCB, and (d) TCB.
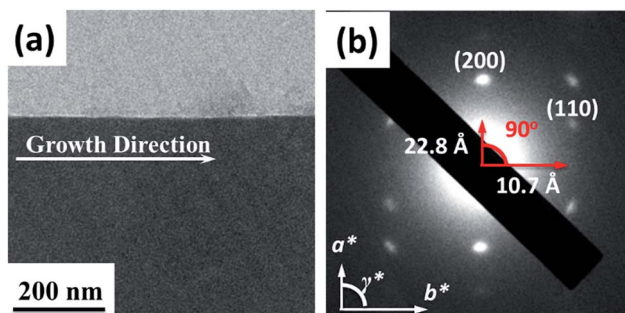

Fig. 3 (a) TEM image and (b) the enlarged ED pattern of the TPA–C$_{60}$ crystal array prepared *via* the PAC method using TCB as solvent.
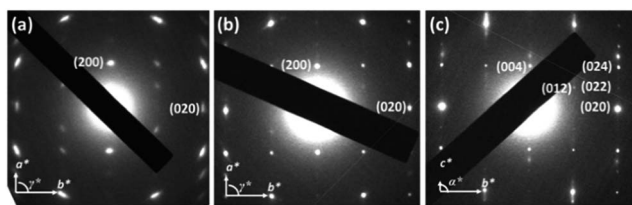
Fig. 4 ED patterns of **TPA–C$_{60}$** crystal prepared from (a) the PAC method, (b) and (c) by drop-casting. Projections of the $a*b*$ and the $b*c*$ reciprocal lattices can be observed in (b) and (c).

and is shown in Fig. 5. The simulated ED patterns (Fig. S8†) generated from the [001] and [100] zones of the model resemble the experimental ones in Fig. 5, showing the validity of the model. The lattice of **TPA–C$_{60}$** features a dual-channel structure containing continuous but separated 2D n-type C$_{60}$ sheets and p-type TPA sheets (Fig. 5b). It is noteworthy that the C$_{60}$-to-C$_{60}$ distance along the a axis (11.4 Å) is different from that along the b axis (10.7 Å). The ED pattern of the crystal array prepared by PAC (Fig. 4a) shares the zone axis, [001], with the pattern in Fig. 4b. Thus, it is confirmed that in the PAC method, the growth direction of the crystal array is along the b axis of the **TPA–C$_{60}$** lattice, and the 2D C$_{60}$ and TPA sheets adopt a flat-on orientation of the substrate.

2.5. Optical and electrochemical properties

The UV-Vis absorption spectrum and cyclic voltammogram (CV) of **TPA–C$_{60}$** are shown in Fig. S9 and S10.† For comparison, the absorption spectra and the CVs of [6,6]-phenyl-C$_{61}$-butyric acid methyl ester (PCBM) and **TPA-OH** are also included in the figures. As shown in Fig. S6,† the absorption maximum of **TPA–C$_{60}$** is similar to that of PCBM. The slightly stronger absorption at 315 nm was attributed to the TPA moiety of **TPA–C$_{60}$**.
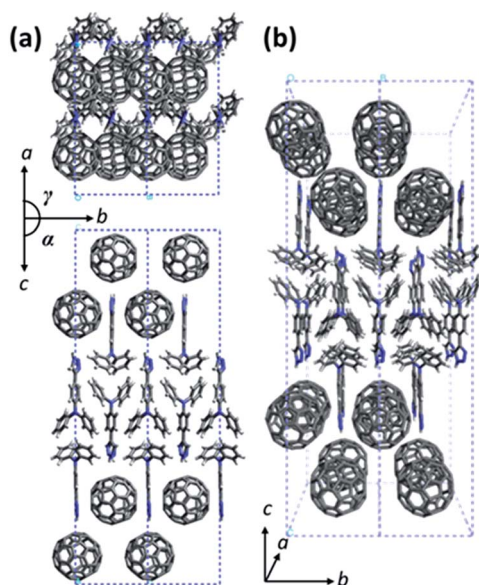

Fig. 5 The lattice model of **TPA–C$_{60}$**. (a) The ab and the bc lattice projections and (b) the projection view of the lattice.

Fig. S10† shows three reversible reductions and one oxidation. The reduction potential, oxidation potential, and HOMO and LUMO energies of the three compounds are summarized in Table S2.† The HOMO and LUMO energies of **TPA–C$_{60}$** are close to the HOMO energy of **TPA-OH** and the LUMO energy of PCBM, suggesting that the C$_{60}$ and TPA moieties of **TPA–C$_{60}$** retain their individual characteristics in the molecule.

2.6. OFET performance

The charge transport properties of the oriented **TPA–C$_{60}$** crystal arrays prepared by the PAC method were investigated in OFET devices with a bottom-gate, top-contact configuration. Because the ED results confirmed that the b lattice axis of **TPA–C$_{60}$** is parallel to the crystal growth direction induced by PAC, as shown in Fig. 6, the source and drain electrodes were arranged parallel or perpendicular to the growth direction, so that the anisotropic charge-transport characteristics of the **TPA–C$_{60}$** crystal arrays along the a and b axes could be studied. The output and transfer plots of the best-performing device are shown in Fig. 7. The **TPA–C$_{60}$** crystal array demonstrated the p-channel characteristics under a negative gate-to-source voltage (V_{GS}) (Fig. 7a) and the n-channel characteristics under a positive V_{GS} (Fig. 7b). The hole mobilities (μ_hs) and electron mobilities (μ_es) deduced from the transfer plots of the devices in saturation regimes are summarized in Table 1. The averaged μ_hs values are 3.37×10^{-4} cm^2 V^{-1} s^{-1} for the parallel devices and 5.43×10^{-5} cm^2 V^{-1} s^{-1} for the perpendicular devices. In the database we have searched, the highest OFET μ_h of a TPA-star burst conjugated molecule was around 3×10^{-4} cm^2 V^{-1} s^{-1}.[37] Thus, the 2D sheets of TPA in the **TPA–C$_{60}$** crystal array retained their hole-transporting ability and delivered one of the best μ_h values among the triarylamine-based molecules. On the other hand, the 2D sheets of the mono-adduct C$_{60}$ delivered averaged μ_es values of 2.11×10^{-4} cm^2 V^{-1} s^{-1} for the parallel devices and 3.54×10^{-5} cm^2 V^{-1} s^{-1} for the perpendicular devices. Thus, the **TPA–C$_{60}$** crystal array has ambipolar charge transport characteristics and delivers balanced hole and electron charge mobilities. Moreover, the anisotropic charge-transport characteristics of the **TPA–C$_{60}$** crystal array are obvious, because the μ_h and μ_e values along the growth direction (b lattice axis) are about one order of magnitude higher than those perpendicular to the growth axis (a lattice axis). The difference can be attributed to shorter TPA–TPA and C$_{60}$–C$_{60}$ distances along the b axis,
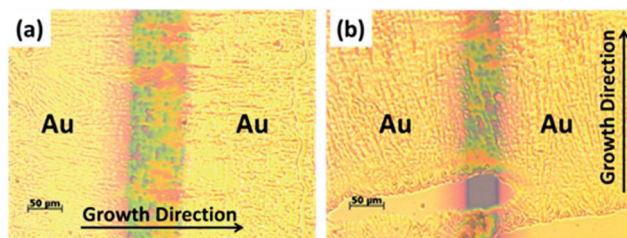

Fig. 6 OM images of the **TPA–C$_{60}$** OFET devices with the gold (Au) source and drain electrodes arranged (a) parallel and (b) perpendicular to the crystal growth direction.
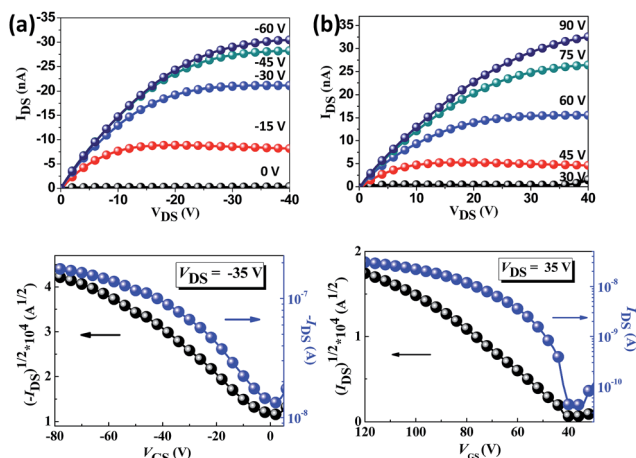
Fig. 7 The output (up) and transfer (down) characteristics of the TPA–C_{60} crystal arrays under (a) negative V_{GS} and (b) positive V_{GS}.

Table 1 OFET characteristics of the TPA−C_{60} crystal arrays[a]

	$\mu_{e\ average}$ (cm^2 V^{-1} s^{-1})	I_{on}/I_{off}	V_{th} (V)	$\mu_{h\ average}$ (cm^2 V^{-1} s^{-1})	I_{on}/I_{off}	V_{th} (V)
Parallel	2.11×10^{-4}	3×10^4	32	3.37×10^{-4}	6×10^3	−22
Perpendicular	3.54×10^{-5}	1×10^1	16	5.43×10^{-5}	2×10^3	−15

[a] The μs values of the parallel devices were averaged from 8 devices, and those of the perpendicular device were averaged from 6 devices.

as shown in the *ab* lattice projection in Fig. 5a. The lower μ_e of the TPA–C_{60} crystal array compared to the best-performing C_{60} OFETs may be related to the longer C_{60}–C_{60} distance and the lower coordination number of C_{60}s in the TPA–C_{60} crystal lattice.[31,38] In addition, the smeared ED pattern in Fig. 4a suggests a certain degree of orientational disorder in the crystal array, which is also detrimental to the μ_e.

3. Conclusions

In summary, a synthetic route for a giant amphiphile (TPA–C_{60}), which is constructed with an amorphous pyramid (TPA) and a crystalline sphere (C_{60}), was developed. DSC results show that the pyramid-sphere-shaped amphiphile forms a solvent-induced ordered phase, because of the strong crystalline nature of the C_{60} moiety. Structural characterization confirmed that TPA–C_{60}s self-assemble into separated 2D C_{60} and TPA sheets in the ordered phase. Processing by the PAC method produced oriented crystal arrays of TPA–C_{60}. ED results indicate that the 2D C_{60} and TPA sheets adopt a flat-on orientation on the substrate with the *b* lattice axis pointing in the crystal growth direction. The flat-on n-type C_{60} nano-sheets and p-type TPA nano-sheets provide electron and hole-transporting channels. Ambipolar and balanced charge-transport characteristics were delivered by the TPA–C_{60} crystal arrays in OFET devices. The dual-channel supramolecular structure of TPA–C_{60} delivered an averaged μ_e of 2.11×10^{-4} cm^2 V^{-1} s^{-1} and a μ_h of 3.37×10^{-4}

cm^2 V^{-1} s^{-1}. The μ_h is comparable to the best-performing tri-arylamine-based p-type conjugated molecules, whereas the modest μ_e delivered by the C_{60} nano-sheets was attributed to the longer C_{60}–C_{60} distance, the lower C_{60} coordination number in the TPA–C_{60} crystal lattice and the less orientational order of the TPA–C_{60} crystal array, compared to the pristine C_{60} crystals. Although a 2D crystal array of C_{60} has been recently disclosed,[39] our study revealed the first example of a dual-channel self-organized structure and the ambipolar characteristics of a novel giant pyramid-sphere-shaped amphiphile.

4. Experimental section

4.1. General measurement and characterization

UV-Vis experiments were carried out using a HITACHI U-4100 spectrophotometer with a 10^{-3} M solution concentration in *o*-dichlorobenzene. The cyclic voltammetry (CV) data were analyzed with a CH Instruments Model 611D with a carbon glass serving as the working electrode and an Ag/Ag$^+$ electrode as the reference electrode, with 0.1 M tetrabutylammonium hexafluorophosphate (Bu$_4$NPF$_6$) as the electrolyte and 10^{-2} M of the desired compound dissolved in *o*-dichlorobenzene. Thermogravimetric analysis (TGA) was conducted on a Perkin-Elmer Pyris under an inert atmosphere with a heating rate of 10 °C min^{-1} and differential scanning calorimetry (DSC) was performed on a TA Q200 Instrument at a temperature ramp rate of 5 °C min^{-1}. For 1D XRD patterns, a Bruker APEX DUO single crystal diffractometer and an APEX II CCD camera equipped with a INCOATEC 18 kW rotating I microfocus X-ray generator (Cu Kα radiation (0.1542 nm)) were used. Transmission Electron Microscopy (TEM) observations were performed on a JEOL JEM-2010 transmission electron microscope with an accelerating voltage of 160 kV and a Gatan-831 CCD camera. Crystal simulation and drawing were based on a Cerius^2 software product from Accelrys.

4.2. OFET fabrication

A n-type heavily doped Si wafer with a SiO$_2$ layer of 300 nm and a capacitance of 11.5 nF cm^{-2} as the gate electrode and dielectric layer was ultrasonically cleaned sequentially in detergent, water and isopropyl alcohol. N-Octadecyltrichlorosilane (ODTS) was used as a self-assembled monolayer. The TPA–C_{60} crystal arrays were prepared *via* the PDMS-assisted crystallization (PAC) method.[31] The gold source and drain electrodes (40 nm in thickness) were then deposited on the organic layer by vacuum evaporation through a shadow mask, affording a bottom-gate, top-contact device configuration. OFET measurement was carried out at room temperature under a nitrogen atmosphere using an Agilent Technologies 4156C instrument. The mobility calculation was based on the equation $I_{ds} = (W/2L)\mu C_i(V_g - V_t)^2$ in the saturation regime, where I_{ds} is the drain–source current, W is the channel width (1 mm), L is the channel length (100 μm), μ is the field-effect mobility, C_i is the capacitance per unit area of the dielectric layer, V_g is the gate voltage, and V_t is the threshold voltage.

4.3. Synthesis

All chemicals were purchased from Aldrich, Acros or TCI and used as received unless specified otherwise. ^1H and ^{13}C NMR spectra were obtained in deuterium-substituted chloroform, $CDCl_3$, as the reference with 0.5 wt% TMS, using Varian 400 MHz spectrometers.

4.4. 8-(4-(Triphenylamino)-1*H*-1,2,3-triazol-1-yl)octan-1-ol (TPA-OH)

To a solution of 4-ethynyl-*N,N*-diphenylaniline **3** (0.5 g, 1.86 mmol), copper(II) sulfate pentahydrate (0.046 g, 0.184 mmol) and sodium ascorbate (0.11 g, 0.56 mmol) was added 8-azidooctan-1-ol **5** (0.382 g, 2.23 mmol) in THF/H_2O 50 ml (1/1, v/v). The reaction mixture was stirred at room temperature for 3 hours then extracted with dichloromethane and water. The organic layer was collected and dried with $MgSO_4$. After removal of the solvent under reduced pressure, the residue was purified by silica gel chromatography with ethyl acetate/hexane (1/3, v/v) as the eluent to give a beige solid (0.55 g, 67%). ^1H NMR (400 MHz, $CDCl_3$): δ 1.31–1.34 (m, 8H), 1.54 (t, 2H, $J = 7$ Hz), 1.93 (t, 2H, $J = 7$ Hz), 3.62 (t, 2H, $J = 6.6$ Hz), 4.37 (t, 2H, $J = 7.2$ Hz), 7.02 (t, 2H, $J = 7.2$ Hz), 7.12 (d, 6H), 7.24 (d, 2H), 7.26 (d, 2H), 7.66 (d, 2H), 7.69 (s, 1H). ^{13}C NMR ($CDCl_3$, 100 MHz): δ 25.6, 26.4, 28.9, 29.1, 30.3, 32.6, 50.3, 62.9, 118.8, 123.0, 123.8, 124.5, 124.7, 126.6, 129.3, 147.5, 147.7. MS (EI, $C_{28}H_{32}N_4O$): calcd, 440.58; found, 440.5.

4.5. 8-(4-(Triphenylamino)-1*H*-1,2,3-triazol-1-yl)octyl acetate C_{60} (TPA–C_{60})

To a solution of **C_{60}-COOH** (70 mg, 0.09 mmol), *p*-toluenesulfonic acid (17 mg, 0.09 mmol), 4-dimethylaminopyridine (11 mg, 0.09 mmol) and 1-(3-dimethylaminopropyl)-2-ethylcarbodiimide hydrochloride (17 mg 0.09 mmol) was added 8-(4-(triphenylamino)-1*H*-1,2,3-triazol-1-yl)octan-1-ol (60 mg, 13.6 mmol) in carbon disulfide (20 ml), the reaction mixture was stirred at room temperature for 12 hours. After removal of the solvent under reduced pressure, the residue was purified by neutral aluminum oxide chromatography with toluene to give a brown solid (79 mg, 74%). ^1H NMR (400 MHz, $CDCl_3$): δ 1.30–1.59 (m, 8H), 1.85 (t, 2H, $J = 7.4$ Hz), 1.95 (t, 2H, $J = 7.4$ Hz), 4.38 (t, 2H, $J = 7.2$ Hz), 4.45 (t, 2H, $J = 6.6$ Hz), 4.78 (s, 1H), 7.02 (t, 2H, $J = 7.2$ Hz), 7.10 (d, 6H), 7.24 (d, 2H), 7.26 (d, 2H), 7.67 (d, 2H), 7.69 (s, 1H). ^{13}C NMR ($CDCl_3$, 100 MHz): δ 25.9, 26.4, 28.6, 30.0, 30.4, 39.1, 50.3, 66.4, 70.6, 77.2, 118.8, 123.0, 123.8, 124.5, 124.8, 126.6, 129.3, 136.4, 140.4, 140.9, 141.1, 142.0, 142.1, 142.2, 142.4, 142.8, 143.0, 143.1, 143.2, 143.7, 143.9, 144.4, 144.6, 144.7, 145.0, 145.1, 145.2, 145.3, 145.6, 145.8, 147.5, 147.6, 147.7, 148.3, 166.4; MS ($C_{90}H_{32}N_4O_2$): calcd, 1201.24; found (FAB), 1200.9; found (MALDI-TOF), 1201.267.

Acknowledgements

Notes and references

1 W.-B. Zhang, X. Yu, C.-L. Wang, H.-J. Sun, I. F. Hsieh, Y. Li, X.-H. Dong, K. Yue, R. van Horn and S. Z. D. Cheng, *Macromolecules*, 2014, **47**, 1221–1239.

2 S. C. Glotzer, *Science*, 2004, **306**, 419–420.

3 F. A. Teng, Y. Cao, Y. J. Qi, M. Huang, Z. W. Han, S. Z. Cheng, W. B. Zhang and H. Li, *Chem.–Asian J.*, 2013, **8**, 1223–1231.

4 J. Baffreau, L. Ordronneau, S. Leroy-Lhez and P. Hudhomme, *J. Org. Chem.*, 2008, **73**, 6142–6147.

5 W.-S. Li, Y. Yamamoto, T. Fukushima, A. Saeki, S. Seki, S. Tagawa, H. Masunaga, S. Sasaki, M. Takata and T. Aida, *J. Am. Chem. Soc.*, 2008, **130**, 8886–8887.

6 C.-L. Wang, W.-B. Zhang, H.-J. Sun, R. M. van Horn, R. R. Kulkarni, C.-C. Tsai, C.-S. Hsu, B. Lotz, X. Gong and S. Z. D. Cheng, *Adv. Energy Mater.*, 2012, **2**, 1375–1382.

7 C.-L. Wang, W.-B. Zhang, X. Yu, K. Yue, H.-J. Sun, C.-H. Hsu, C.-S. Hsu, J. Joseph, D. A. Modarelli and S. Z. D. Cheng, *Chem.–Asian J.*, 2013, **8**, 947–955.

8 S. V. Kirner, D. M. Guldi, J. D. Megiatto Jr and D. I. Schuster, *Nanoscale*, 2015, **7**, 1145–1160.

9 D. I. Schuster, P. D. Jarowski, A. N. Kirschner and S. R. Wilson, *J. Mater. Chem.*, 2002, **12**, 2041–2047.

10 H. Imahori, *Org. Biomol. Chem.*, 2004, **2**, 1425–1433.

11 R. Chitta and F. D'Souza, *J. Mater. Chem.*, 2008, **18**, 1440–1471.

12 S. V. Kirner, D. Arteaga, C. Henkel, J. T. Margraf, N. Alegret, K. Ohkubo, B. Insuasty, A. Ortiz, N. Martín and L. Echegoyen, *Chem. Sci.*, 2015, **6**, 5994–6007.

13 H. Hayashi, W. Nihashi, T. Umeyama, Y. Matano, S. Seki, Y. Shimizu and H. Imahori, *J. Am. Chem. Soc.*, 2011, **133**, 10736–10739.

14 H. Imahori, T. Umeyama, K. Kurotobi and Y. Takano, *Chem. Commun.*, 2012, **48**, 4032–4045.

15 F. Wessendorf, B. Grimm, D. M. Guldi and A. Hirsch, *J. Am. Chem. Soc.*, 2010, **132**, 10786–10795.

16 G. Liu, A. N. Khlobystov, G. Charalambidis, A. G. Coutsolelos, G. A. Briggs and K. Porfyrakis, *J. Am. Chem. Soc.*, 2012, **134**, 1938–1941.

17 D. I. Schuster, K. Li, D. M. Guldi, A. Palkar, L. Echegoyen, C. Stanisky, R. J. Cross, M. Niemi, N. V. Tkachenko and H. Lemmetyinen, *J. Am. Chem. Soc.*, 2007, **129**, 15973–15982.

18 P. A. Liddell, G. Kodis, A. L. Moore, T. A. Moore and D. Gust, *J. Am. Chem. Soc.*, 2002, **124**, 7668–7669.

19 M. Wolffs, F. J. Hoeben, E. H. Beckers, A. P. Schenning and E. Meijer, *J. Am. Chem. Soc.*, 2005, **127**, 13484–13485.

20 R. W. Date and D. W. Bruce, *J. Am. Chem. Soc.*, 2003, **125**, 9012–9013.

21 G. Bottari, G. de la Torre, D. M. Guldi and T. S. Torres, *Chem. Rev.*, 2010, **110**, 6768–6816.

22 L. Cui, J. P. Collet, G. Xu and L. Zhu, *Chem. Mater.*, 2006, **18**, 3503–3512.

23 H. Araki and K. Naka, *J. Polym. Sci., Part A: Polym. Chem.*, 2012, **50**, 4170–4181.

24 R. Charvet, Y. Yamamoto, T. Sasaki, J. Kim, K. Kato, M. Takata, A. Saeki, S. Seki and T. Aida, *J. Am. Chem. Soc.*, 2012, **134**, 2524–2527.

25 H. Imahori, D. M. Guldi, K. Tamaki, Y. Yoshida, C. Luo, Y. Sakata and S. Fukuzumi, *J. Am. Chem. Soc.*, 2001, **123**, 6617–6628.

26 P. F. Damasceno, M. Engel and S. C. Glotzer, *Science*, 2012, **337**, 453–457.

27 D. F. O'Brien, P. E. Burrows, S. R. Forrest, B. E. Koene, D. E. Loy and M. E. Thompson, *Adv. Mater.*, 1998, **10**, 1108–1112.

28 P. Strohriegl and J. V. Grazulevicius, *Adv. Mater.*, 2002, **14**, 1439–1452.

29 C.-Y. Chang, L. Zuo, H.-L. Yip, Y. Li, C.-Z. Li, C.-S. Hsu, Y.-J. Cheng, H. Chen and A. K. Y. Jen, *Adv. Funct. Mater.*, 2013, **23**, 5084–5090.

30 M. M. Lee, J. Teuscher, T. Miyasaka, T. N. Murakami and H. J. Snaith, *Science*, 2012, **338**, 643–647.

31 K.-Y. Wu, T.-Y. Wu, S.-T. Chang, C.-S. Hsu and C.-L. Wang, *Adv. Mater.*, 2015, **27**, 4371–4376.

32 L. Y. Chiang, P. A. Padmawar, T. Canteenwala, L.-S. Tan, G. S. He, R. Kannan, R. Vaia, T.-C. Lin, Q. Zheng and P. N. Prasad, *Chem. Commun.*, 2002, 1854–1855.

33 D. Konarev, A. Y. Kovalevsky, A. Litvinov, N. Drichko, B. Tarasov, P. Coppens and R. Lyubovskaya, *J. Solid State Chem.*, 2002, **168**, 474–485.

34 S. Clavaguera, S. I. Khan and Y. Rubin, *Org. Lett.*, 2009, **11**, 1389–1391.

35 B. Ma, C. E. Bunker, R. Guduru, X.-F. Zhang and Y.-P. Sun, *J. Phys. Chem. A*, 1997, **101**, 5626–5632.

36 H.-S. Kitzerow and C. Bahr, *Chirality in Liquid Crystals*, Springer-Verlag, New York, 2001, ch. 7, p. 186.

37 M. Sonntag, K. Kreger, D. Hanft, P. Strohriegl, S. Setayesh and D. de Leeuw, *Chem. Mater.*, 2005, **17**, 3031–3039.

38 H. Li, B. C. Tee, J. J. Cha, Y. Cui, J. W. Chung, S. Y. Lee and Z. Bao, *J. Am. Chem. Soc.*, 2012, **134**, 2760–2765.

39 X. Zhang, C. H. Hsu, X. Ren, Y. Gu, B. Song, H. J. Sun, S. Yang, E. Chen, Y. Tu, X. Li, X. Yang, Y. Li and X. Zhu, *Angew. Chem., Int. Ed.*, 2015, **54**, 114–117.